PCCP

RSC Publishing

PAPER

View Article Online
View Journal | View Issue

Cite this: *Phys. Chem. Chem. Phys.*, 2013, **15**, 19387

Enhanced photosensitized activity of a BiOCl–Bi_2WO_6 heterojunction by effective interfacial charge transfer†

Wenjuan Yang,[a] Bo Ma,[a] Weichao Wang,[b] Yanwei Wen,[a] Dawen Zeng*[a] and Bin Shan*[ac]

Received 27th August 2013,
Accepted 29th September 2013

DOI: 10.1039/c3cp53628a

www.rsc.org/pccp

A BiOCl–Bi_2WO_6 heterojunction with a chemically bonded interface was synthesized *via* a facile one-step solvothermal method. A series of characterization techniques (XRD, XPS, TEM, SEM, EDS *etc.*) confirmed the existence of a BiOCl–Bi_2WO_6 interface. The heterojunction yielded a higher photodegradation rate of Rhodamine B under visible light irradiation compared to its individual components. Theoretical studies based on density functional theory calculations indicated that the enhanced photosensitized degradation activity could be attributed to the favorable band offsets across the Bi_I–O–Bi_{II} bonded interface, leading to efficient interfacial charge carrier transfer. Our results reveal the photosensitized mechanism of BiOCl–Bi_2WO_6 heterojunctions and demonstrate their practical use as visible-light-driven photocatalytic materials.

1. Introduction

Semiconductor photocatalysis has been put forward as an effective strategy for organic pollutant remediation and water splitting. The critical obstacle that limits its industrialization arises from the lack of low-cost and high efficient semiconductor photocatalytic materials and photoelectrodes.[1,2] Bismuth-based photocatalytic materials such as BiOCl,[3–6] Bi_2WO_6,[7–11] $BiVO_4$,[12,13] $BiNbO_4$[14] *etc.* have recently aroused great interest in the scientific community due to their intriguing electronic structures.[15] Among these compounds, bismuth oxyhalides with layered structures show great promise owing to their mechanical robustness, outstanding photocatalytic activities and chemical stability. In particular, BiOCl,[16] which has a layered structure consisting of $[Bi_2O_2]^{2+}$ layers sandwiched between two sheets of Cl ions with an internal electric field along the [001] direction, has been demonstrated to show superior photocatalytic performance under ultraviolet light irradiation.[3,17] However, due to its large indirect band gap of about 3.40 eV, the pure phase of intrinsic BiOCl has limited photocatalytic activity under visible light. Photosensitization caused by dye, permitting expansion of the wavelength response of BiOCl, has been proved to be one of the promising ways for the visible photodegradation and mineralization of dye pollutants.[18,19] While a few groups reported relatively high quantum efficiencies in certain photosensitization reactions,[20,21] its quantum efficiency and conversion ratio generally remain low. Therefore, it is expected that forming heterojunction structures may be an effective appropriate solution to the problem.[22–30] Huang *et al.*[30] successfully fabricated a Bi_2S_3–BiOCl heterojunction by a controlled anion exchange approach to display highly efficient visible light photoactivities. The heterojunction may promote the interfacial charge transfer (IFCT), which can minimize electron–hole recombination, thus significantly enhancing energy transfer efficiency. Among bismuth-based materials, Bi_2WO_6 is chosen as a promising candidate to form a BiOCl–Bi_2WO_6 heterojunction owing to the following advantages: (I) the crystal lattice of Bi_2WO_6 matches well with that of BiOCl, implying the epitaxial growth of one phase over the other with little strain at the interface.[31] (II) The Bi_2WO_6 catalyst (band gap of 2.7 eV)[9] can absorb visible light, extending the light-absorbance capability of the composite catalyst. (III) The Bi_2WO_6 catalyst as a direct band gap semiconductor could generate electron–hole pairs efficiently. While many recent works focused on the photocatalytic behavior of individual components separately,[3,4,9] there are few detailed reports on the fabrication method, optical properties or photosensitized degradation activity (PSDA) of dye for the BiOCl–Bi_2WO_6 heterojunction. What is more, the charge transfer mechanism at the interface still remains unknown. These questions deserve further investigation.

In this study, we report the fabrication of the BiOCl–Bi_2WO_6 heterojunction *via* a facile solvothermal method. The structural features of the heterojunction were confirmed using XRD, XPS,

[a] *State Key Laboratory of Material Processing and Die and Mould Technology and School of Materials Science and Technology, Huazhong University of Science and Technology, Wuhan 430074, China. E-mail: dwzeng@mail.hust.edu.cn, bshan@mail.hust.edu.cn; Fax: +86-27-87542857; Tel: +86-27-87542857*
[b] *Department of Electronics, Nankai University, Tianjin 300071, China*
[c] *Department of Materials Science and Engineering, The University of Texas at Dallas, Richardson, Texas 75080, USA*

† Electronic supplementary information (ESI) available: Surface energy calculations. See DOI: 10.1039/c3cp53628a

TEM, SEM, EDS *etc.* characterization techniques. A nanostructured BiOCl–Bi_2WO_6 heterojunction showed superior photosensitized degradation activity of RhB and photoelectrochemical (PEC) properties to those of pure phases. The results are in contrast to our former theoretical predictions[31] that band offsets (BOs) of a BiOCl–Bi_2WO_6 heterojunction might not be favorable for the electron–hole separation. However, further investigation reveals that the discrepancy can be attributed to the difference in the interface atom species which greatly affects the stability and photocatalytic performance.[32] By taking account of the surface energy stability analysis that was neglected in the previous theoretical model, the more likely formed interface during the growth of heterojunctions is determined to be Bi_I–O–Bi_{II}. The BOs of this stable heterojunction show a favorable alignment for chemically bonded interfacial charge transfer (CB-IFCT), which agrees with our experimental results of the enhanced PSDA of RhB.

2. Experimental and simulation details

2.1. Sample preparations

All chemicals used were the analytical-grade reagents without any further purification. The BiOCl–Bi_2WO_6 composite was synthesized *via* a solvothermal process, using ethylene glycol (EG) without water as solution. Firstly, 0.001 mol WCl_6 and 0.002 mol $Bi(NO_3)_3{\cdot}5H_2O$ were dissolved in 50 ml EG by ultrasonication for about 10 minutes and stirred at the room temperature until all reactants were dissolved. Then 0.020 mol urea was added to the solution by stirring until it dissolved fully. When the solution became colorless and clear, the solution was transferred into 80 ml Teflon-lined stainless steel autoclaves. The autoclaves were sealed and maintained at a constant temperature of 120 °C, 150 °C, 180 °C, respectively. The samples were subsequently cooled to ambient temperature naturally in the oven. The reaction conditions and corresponding sample species could be found in Table 1. All generated samples were obtained by filtering and washing with ethanol and deionized water for 3–5 times to remove EG and impurity ions. Finally, the products were dried at 90 °C for 10 h in the oven.

2.2. Characterization

The crystal structures of the as-synthesized powders were characterized by X-ray diffraction, recorded on an analytical X'pert PRO diffractometer, using Cu Kα radiation with λ = 1.5406 Å in the 2θ ranging from 10° to 80°. The surface compositions and chemical states were examined by XPS performed on an ESCALAB 250 photoelectron spectroscope (Thermo Fisher Scientific Inc.) using Mg Kα radiation. The morphology and structure characterization of fabricated composites were conducted on field-emission scanning electron microscopy (FE-SEM, FEI, Sirion 200 microscope, operated at an acceleration voltage of 20.0 kV) with energy dispersive X-ray spectroscopy (EDS, Inca X-Max 50) and high-resolution transmission electron microscopy (HRTEM, JEOL-2010, FEF; 200 KV), respectively. The optical band gaps of the powders were measured by UV-vis diffuse reflection spectra which were obtained on a Lambda 35 UV-vis spectrometer (PerkinElmer Co., Ltd., USA) with scanning wavelength ranging from 250 nm to 800 nm and a reference of $BaSO_4$.

Table 1 Reaction conditions, photosensitized degradation parameters of RhB, photocurrent density and impedance parameters (after fitting) of the cells based on BiOCl, Bi_2WO_6, BiOCl–Bi_2WO_6 samples

Sample	Temperature (°C)	Time (h)	PDP[a] (%)	PDR[a] (min^{-1})	PCD[a] ($\mu A\ cm^{-2}$)	R_{ct} (Ω)
BiOCl	120	15	74.3	0.029	0.18	30 653
BiOCl–Bi_2WO_6	150	25	84.6	0.059	0.30	9133
Bi_2WO_6	180	15	72.0	0.041	0.20	13 986

[a] PDP, PDR and PCD are abbreviations for photodegradation percentage of RhB, photodegradation rates and photocurrent density, respectively.

2.3. Photocatalytic and photoelectrochemical measurements

The photocatalytic activities were evaluated by the degradation of RhB using a round-bottomed beaker with a water circulating pump. The reaction mixture was illuminated with a visible-light source of a 350 W Xe lamp (an illumination intensity of 100 mW cm^{-2} recorded using a Solar Power Meter (TES 1333)). In each test, 0.1 g of the catalyst was added to 200 ml RhB (20 mg L^{-1}) and magnetically stirred for one hour in the dark in order to attain the adsorption–desorption equilibrium. When photodegradation experiment began, 4 ml solution was extracted from the reaction solution at fixed-time intervals, further centrifuged to remove catalyst powders and finally analyzed using a UV-2550 spectrophotometer. The characteristic absorption peak of RhB at 553 nm was measured to determine the concentration of RhB with the reference sample of deionized water.

The fluorine doped tin oxide (FTO) substrates were cleaned by ultrasonication in distilled water, absolute ethanol and isopropanol for 20 min sequentially. The conducting glass substrates were covered and kept area of 1 cm^2 with high-temperature resistant adhesive tape. Typically, the aqueous slurries of the BiOCl, Bi_2WO_6 and BiOCl–Bi_2WO_6 samples were spread on a FTO glass substrate by the spin coating method. The aqueous slurries were fabricated by grinding 50 mg of the BiOCl, Bi_2WO_6 and BiOCl–Bi_2WO_6 samples, 40 μL of PEDOT-PSS (Sigma-Aldrich, 1.3–1.7%) aqueous solution and 200 μL of water. The films were dried in air and then annealed at 150 °C for 10 min. The photoelectrochemical properties were measured using an electrochemical analyzer (Correst 310 Instruments) in a standard three-electrode system with the BiOCl, Bi_2WO_6 and BiOCl–Bi_2WO_6 samples as the working electrodes, a Pt foil as the counter electrode and a saturated Ag/AgCl as a reference electrode under simulated sunlight illumination. A 0.5 M Na_2SO_4 aqueous solution was used as the electrolyte. Electrochemical impedance spectra (EIS) measurements were performed and analyzed by ZView software.

2.4. Computational methods

Our calculations were based on the density functional theory (DFT) with the Perdew–Burke–Ernzerhof[33] parameterization of

generalized gradient approximation (GGA-PBE) for the exchange–correlation potential. We used the projector-augmented-wave (PAW)[34] method as implemented in a plane-wave basis code VASP.[35,36] An energy cutoff of 400 eV and 7 × 7 × 1 Γ centered k-points were utilized in the calculations of BiOCl–Bi_2WO_6 heterojunction parameters. The magnitude of force on each atom was converged to 0.01 eV $Å^{-1}$. All atomic coordinates were fully relaxed and the interface distances were optimized using the conjugate gradient method.[37]

The unit cell for BiOCl is a tetragonal structure with lattice constants $a = b = 3.890$ Å and $c = 7.890$ Å.[16] For Bi_2WO_6, the lattice constants are $a = 5.437$ Å, $b = 16.433$ Å and $c = 5.459$ Å.[38] An interface model of BiOCl (001) and Bi_2WO_6 (010) planes was built based on HRTEM results. To compensate the lattice constant difference, the (001)-oriented BiOCl was rotated counter-clockwise by 45° to match with the lattice of the Bi_2WO_6 (010) plane with a small lattice strain (1.16%). Two unit cells of BiOCl and two unit cells of Bi_2WO_6 were used along the interface for the heterojunction model. A 10 Å vacuum region was adopted to avoid the interactions between top and bottom atoms in the periodic slab images. Half the amount of oxygen atoms was removed from Bi_2WO_6 surfaces to fully passivate the exposed surfaces.[31] The whole slab was 40.26 Å thick and consisted of 84 atoms in total.

3. Results and discussion

3.1 Structural characterization of the BiOCl–Bi_2WO_6 heterojunction

The crystal structures of products synthesized at different reaction temperatures (120 °C, 150 °C, 180 °C) were characterized by XRD (Fig. 1). For the samples synthesized at 120 °C and 180 °C, the XRD peaks correspond to pure phase BiOCl (JCPDS no. 006-0249) and Bi_2WO_6 (JCPDS no. 039-0256), respectively. For the sample at 150 °C, two series of XRD peaks can be observed. Those diffraction peaks with 2θ = 11.97°, 25.86°, 32.50°, 41.50°, 46.64° and 54.09° could be indexed to the (001), (101), (110), (112), (200) and (211) crystal faces of BiOCl, while additional diffraction peaks

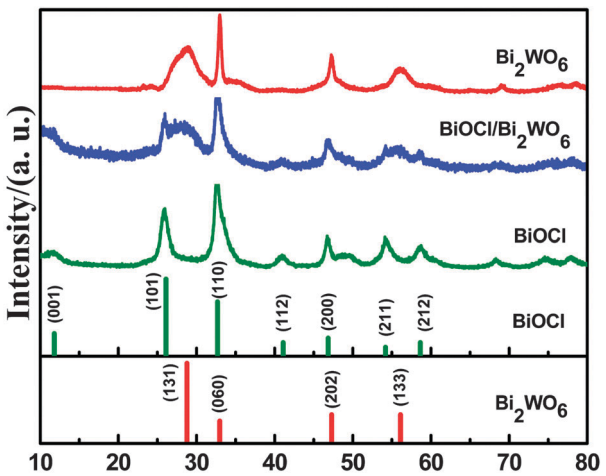

Fig. 1 Wide-angle XRD patterns of synthesized samples: BiOCl, Bi_2WO_6 and BiOCl–Bi_2WO_6.

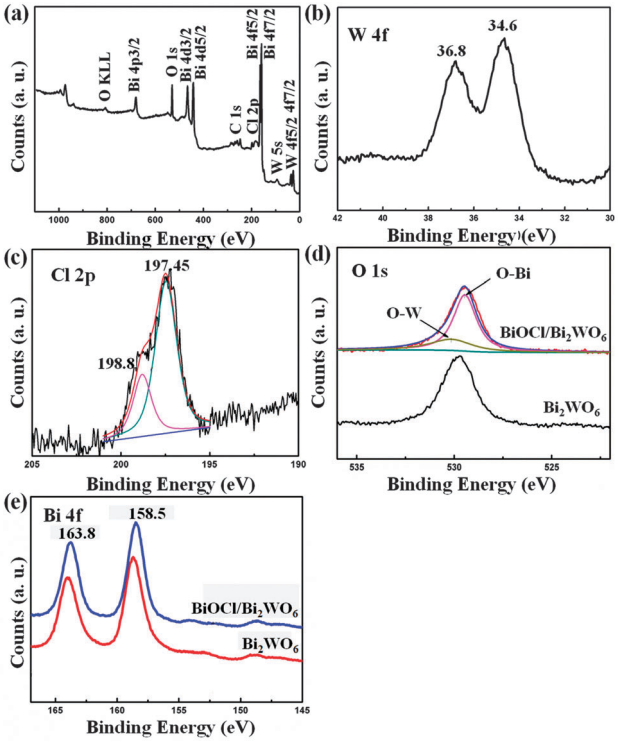

Fig. 2 (a) Whole pattern of the heterojunction BiOCl–Bi_2WO_6 XPS spectrum, (b) W 4f of BiOCl–Bi_2WO_6, (c) Cl 2p of BiOCl–Bi_2WO_6, (d) O 1s of pure Bi_2WO_6 and BiOCl–Bi_2WO_6, (e) Bi 4f of pure Bi_2WO_6 and BiOCl–Bi_2WO_6. Among them, Cl 2p peaks were fitted into two peaks located at 198.80 eV and 197.45 eV, respectively. O 1s peaks were attributed to the coordination of oxygen in Bi–O and W–O, respectively.

with 2θ values of 28.30°, 32.67°, 46.97° and 56.50° corresponding to (131), (060), (202) and (133) crystal planes of Bi_2WO_6. The XRD analysis indicates the co-existence of BiOCl and Bi_2WO_6 phases in the solvothermal synthesized products at a temperature of 150 °C. No other new phases are observed in the XRD patterns.

To identify surface compositions and chemical states of the composite photocatalysts, the heteroarchitectural BiOCl–Bi_2WO_6 was analyzed by XPS measurements. The binding energies in the spectrum were calibrated using that of C 1s (284.62 eV). Fig. 2(a) shows the whole pattern of the BiOCl–Bi_2WO_6 heterojunction's XPS spectrum. In Fig. 2(b), two peaks locating at 34.60 eV and 36.80 eV belong to W 4f peaks.[39,40] Cl 2p peaks, shown in Fig. 2(c), are divided into two peaks 197.45 eV and 198.80 eV, which can be assigned to the Cl $2p_{3/2}$ and Cl $2p_{1/2}$ region, respectively. The O 1s peaks for the BiOCl–Bi_2WO_6 heterostructure in Fig. 2(d) come from overlapping contributions of oxide ions O^{2-}, which can be Gaussian fitted into two peaks: at 529.50 eV and 530.20 eV. The peak on the lower binding energy side of the O 1s spectrum could be attributed to the coordination of oxygen in Bi–O,[16,26] while the higher binding energy centered at 530.20 eV could be attributed to the coordination of oxygen in W–O.[41] In Fig. 2(e) the binding energies for Bi $4f_{7/2}$ and Bi $4f_{5/2}$ are 158.50 and 163.80 eV, which could be assigned to Bi^{3+} ions,[16,26] both of which, as well as O peaks, have a small shift to the lower energy region compared with those of pure

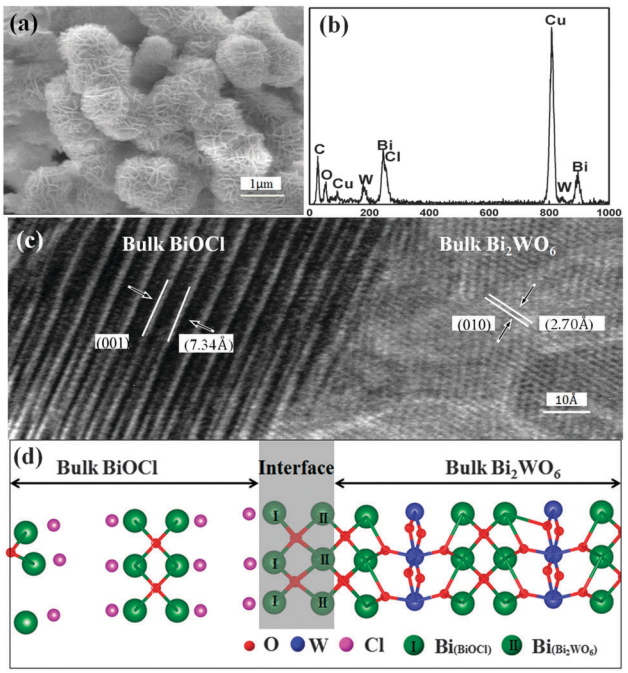

Fig. 3 (a) Representative FE-SEM image of BiOCl–Bi_2WO_6, (b) EDS image of BiOCl–Bi_2WO_6 with Bi, W, Cl, O atoms, (c) high magnification HRTEM image of interface BiOCl with the exposed (001) plane and Bi_2WO_6 with the exposed (010) plane, (d) ball and stick model of the BiOCl–Bi_2WO_6 heterojunction. Pink, green, red and blue atoms represent Cl, Bi, O, and W, respectively.

Bi_2WO_6 owing to the influence of low energy of Bi–O bonding from BiOCl. These indicate the interaction between BiOCl and Bi_2WO_6 with chemical bonding in the composite catalyst.

The microstructures of the obtained samples were also examined with FE-SEM (Fig. 3(a)). The FE-SEM image shows that the photocatalysts consist of a large number of uniform, hierarchical nanostructures like nano-flowers with a size of about 1 μm in diameter and two-dimensional crystalline nanosheets on the surface. Owing to the very similar morphologies of BiOCl and Bi_2WO_6 catalysts, it is hard to visually distinguish the two phases from the FE-SEM image. In order to further confirm the chemical compositions of the mixed BiOCl–Bi_2WO_6 photocatalyst, EDS analysis was performed with its spectrum shown in Fig. 3(b). It can be seen that the sample was composed of the Bi, W, Cl, O elements, indicating the co-existence of both phases (we note that the signals of Cu and C elements in the spectrum come from the copper grid and conductive tape). To gain further insight into the detailed structure of the heterojunction catalyst, the sample was further characterized by HRTEM. Fig. 3(c) displays an interface region in the BiOCl–Bi_2WO_6 nanosheets-based nanostructures. The border between BiOCl and Bi_2WO_6 planes is distinct, suggesting an intimate contact between the phases. The lattices with periodic fringe spacings of 7.34 Å and 2.70 Å correspond to the interplanar crystal spacing of BiOCl (001) planes and Bi_2WO_6 (010) planes, respectively. These planes also manifest themselves in the XRD peaks at 11.97° and 32.67° of the BiOCl–Bi_2WO_6 catalyst and have also been observed in previous experiments.[19,42] On the basis of the HRTEM results, we built a slab model for simulating the interface between the BiOCl (001) plane and the Bi_2WO_6 (010) plane, as shown in Fig. 3(d). The interface atoms are marked as Bi_I–O–Bi_{II} (where Bi_I refers to Bi atoms in the BiOCl and Bi_{II} refers to Bi atoms in the Bi_2WO_6, detailed information about the model will be discussed in the following sections).

3.2 Optical and photocatalytic properties of the BiOCl–Bi_2WO_6 catalyst

To study the optical response of the obtained samples, the photocatalysts were characterized by a UV-vis spectrum. From the spectrum shown in Fig. 4, the light absorption range of the photocatalyst BiOCl–Bi_2WO_6 heterojunction has a red shift towards the visible-light region compared to the pure BiOCl catalyst, owing to the incorporation of the Bi_2WO_6 catalyst. The optical band gap of the BiOCl–Bi_2WO_6 photocatalyst is deduced from the formula: E_g (eV) = 1240/λ (nm). According to the formula, the optical band gap of the heterojunction is calculated to be about 2.70 eV.

To further understand the effect on the PSDA enhancement of BiOCl–Bi_2WO_6 heterostructures, we carefully studied the photodegradation of RhB for the BiOCl–Bi_2WO_6 heterostructures under visible-light irradiation (λ > 420 nm). Temporal evolution of the absorbance changes at a time interval of 5 minutes was displayed in Fig. 5(a). The concentrations of RhB show sharp decrease in the first 5 minutes, as evidenced by the decrease in absorbance. After 30 minutes of photodegradation reaction, RhB concentration was significantly reduced and kept stable. In Fig. 5(b), we show the RhB concentration changes with time. Note that illumination in the absence of catalysts (1) or dark conditions with catalysts (2) nearly does not result in the photocatalytic decomposition of RhB. Therefore, the presence of both illumination and catalysts are necessary for efficient photodegradation. We show the photodegradation percentage and derived photodegradation rates in Table 1. The amount of RhB decomposed is about 84.6% for the BiOCl–Bi_2WO_6 heterojunction catalyst, 74.3% for BiOCl and 72.0% for Bi_2WO_6. To evaluate

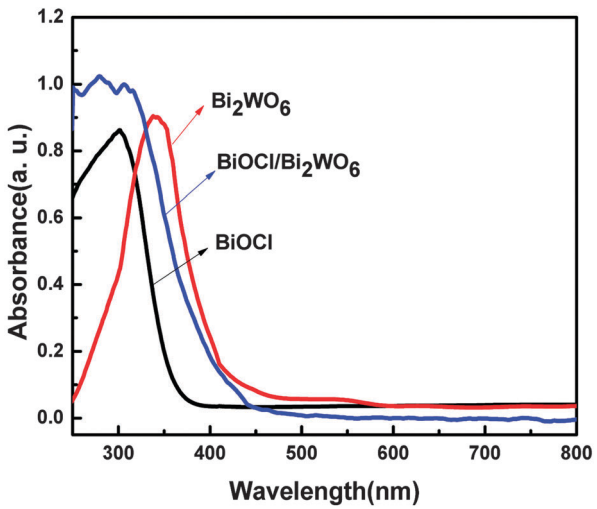

Fig. 4 UV-vis absorbance spectra of BiOCl, Bi_2WO_6 and BiOCl–Bi_2WO_6 photocatalysts in terms of wavelength.

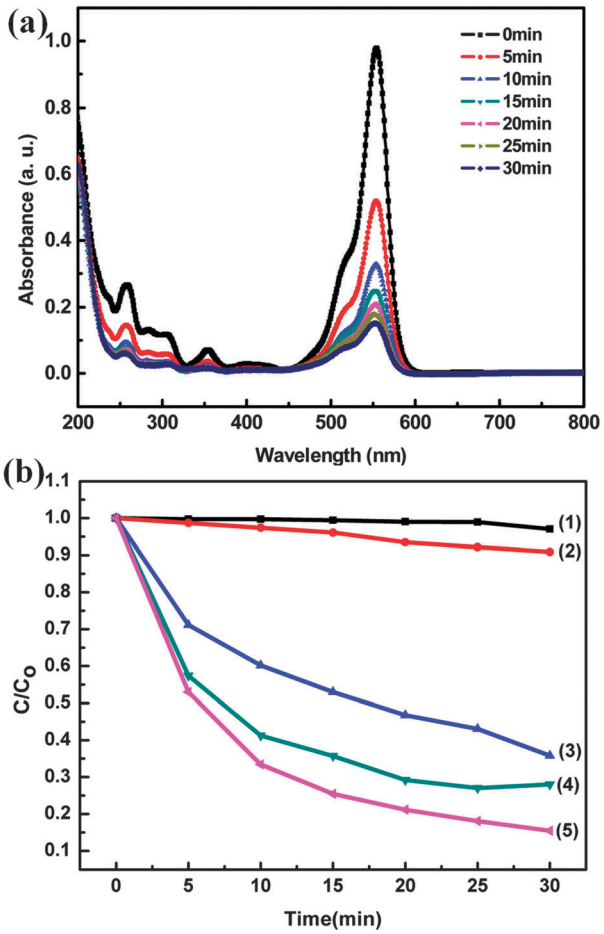

Fig. 5 (a) Temporal evolution of the absorbance curve in the degradation of RhB for the BiOCl–Bi_2WO_6 heterojunction, (b) RhB concentration changes with time (1) illumination in the absence of powder, (2) in the presence of BiOCl–Bi_2WO_6 without light, (3) BiOCl under visible light irradiation, (4) Bi_2WO_6 under visible light irradiation and (5) BiOCl–Bi_2WO_6 under visible light irradiation, respectively.

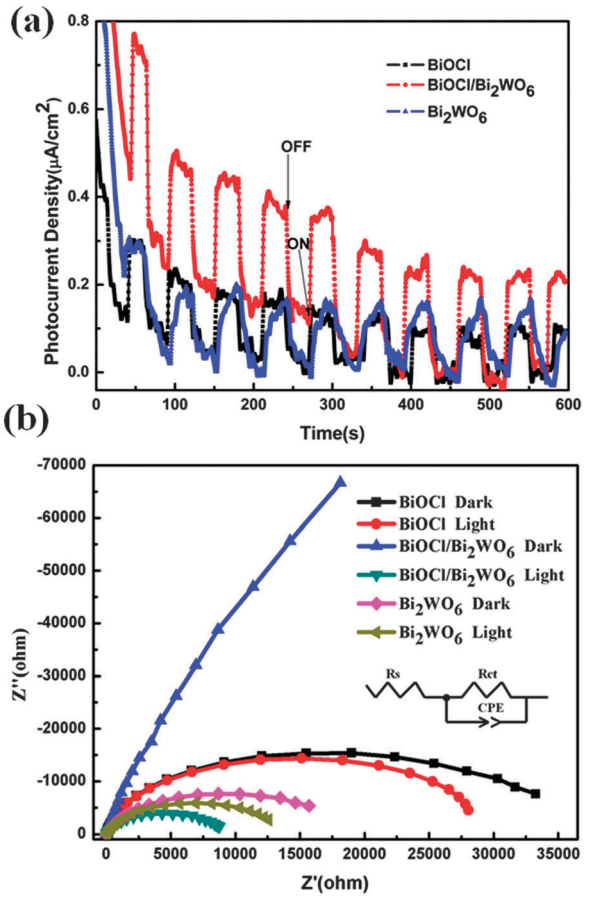

Fig. 6 (a) Transient photocurrent density *vs.* time plotted for the BiOCl, Bi_2WO_6 and BiOCl–Bi_2WO_6 samples in 0.5 M Na_2SO_4 aqueous solutions under UV-vis irradiation at 0.5 V *vs.* Ag/AgCl. (b) Electrochemical impedance Nyquist plots of BiOCl, Bi_2WO_6 and BiOCl–Bi_2WO_6 heterojunction electrodes under dark and light irradiation in the 0.5 M Na_2SO_4 electrolyte. In the equivalent circuit (inset), R_s represents the circuit series-resistance, CPE is the capacitance phase element of the semiconductor–electrolyte interface and R_{ct} is the charge transfer resistance across the interface.

the photocatalytic efficiency quantitatively, the photodegradation rate constants (k) were obtained by fitting the lines of $\ln(C_o/C)$ *vs.* t, assuming that the photochemical reaction follows pseudo first-order kinetics (where C means the concentration of solute remaining in the solution at the irradiation time of t and C_o refers to the initial solution concentration). Degradation rate constants of pure BiOCl and Bi_2WO_6 were calculated to be 0.029 min^{-1} and 0.041 min^{-1}, respectively. The rate constant for BiOCl–Bi_2WO_6 reaches up to 0.059 min^{-1}, which is about twice faster than that of pure BiOCl and one and half times faster than that of Bi_2WO_6.

To investigate the photocurrent properties of the as-synthesized BiOCl, Bi_2WO_6 and BiOCl–Bi_2WO_6 heterostructures, photoresponses were performed under several on/off sunlight irradiation cycles shown in Fig. 6(a). At the beginning, the photocurrent does not reach equilibrium. After about 300 seconds, the photocurrent value becomes stable and decreases to zero as soon as the incident light on the photoanode is turned off and returns to the original value only when the light is turned on again. This indicates rapid IFCT within the photocatalyst. These samples generate photocurrent density with a reproducible response to on/off cycles under pulsed interval illumination, demonstrating that the photoanodes are stable. We list photocurrent density data in Table 1. The BiOCl–Bi_2WO_6 heterojunction exhibited a higher transient photocurrent density (about 0.3 μA cm^{-2}) than those of the Bi_2WO_6 sample and the BiOCl sample by a factor of 1.6 and 2.0, respectively. To gain deeper insight into the IFCT behaviors in the heterojunction system, we compared EIS Nyquist of BiOCl, BiOCl–Bi_2WO_6 and Bi_2WO_6 films (Fig. 6(b)). In dark, all the diagrams were similar, including a macro arc part corresponding to IFCT resistance. The radium of the BiOCl–Bi_2WO_6 arc is the largest among these samples, meaning that the resistance is the largest. Upon irradiation, the radii of the micro semicircle arc become much smaller than those in the dark, which can be attributed to the increased electronic conductivity of the electrodes under irradiation. The deduced equivalent circuit for the photoanodes (inset of Fig. 6(b)) consists of solution resistance (R_s) and charge transfer resistance (R_{ct}) in parallel to the constant phase element (CPE). We obtained the accurate values of R_s, R_{ct}, CPE through fitting

the equivalent circuit. Among these parameters, the R_{ct} indicates the ability of charge transfer. The smaller the R_{ct} is, the better the charge transfer ability is. Under light, the BiOCl–Bi_2WO_6 heterojunction shows the smallest R_{ct} (shown in Table 1), indicating the most effective CB-IFCT, which elucidates its higher PEC activity in Fig. 6(a).

3.3 BOs and the photosensitized mechanism

Based on the HRTEM results, we built an atomistic model representing a BiOCl–Bi_2WO_6 interface. As the HRTEM results indicate the existence of Bi_2WO_6 (010) facets, we first considered the stability of the (010) plane of Bi_2WO_6 with six possible terminations labeled as O_I, Bi_I, WO, O_{II}, Bi_{II}, O_{III} in the side view in Fig. S1(a) (ESI†). In order to determine the most stable surface terminations during crystal growth, we computed their surface grand potentials[43] which were listed in Table SI (ESI†) (computational details can be found in ESI†). With the oxygen chemical potentials ranging from −0.38 to −0.50 eV[44] at our experimental temperature, the O_I terminated surface is thermodynamically most favorable and should be the prevalent exposed facet. Taking this growth kinetics into account, our interfacial model consists of the (010) plane of Bi_2WO_6 with O_I termination, bonded *via* oxygen atoms to the Bi atoms in the (001) plane of BiOCl, forming Bi_I–O–Bi_{II} bonding across the interface as shown in Fig. S1(b) (ESI†). This complements our previous theoretical study where the surface energies during crystal growth were not considered and W–O–Bi interface bonding was assumed based on bond energies only.[31] To gain insight into the improved PSDA of the BiOCl–Bi_2WO_6 heterojunction, we calculated the BOs between the two semiconductor materials since they are some of the key parameters for charge carrier transportation across the interface. The BOs were obtained by LDOS analysis[45,46] and the potential-line-up method.[47–49] These two methods yielded similar results. Fig. 6(a) shows the total density of states (TDOS) and LDOS projected onto different layers along the interface normal. The labels marked "bulk BiOCl" and "bulk Bi_2WO_6" refer to the LDOS of atom layers away from the interface region. It can be seen that the valence band maximum (VBM) of the heterojunction is mainly composed of the VBM of BiOCl, while the conduction band minimum (CBM) of the heterojunction consists of the CBM of Bi_2WO_6. The potential-line-up method was also used to calculate the valence band offset (VBO) according to the formula[50]

$$\mathrm{VBO} = \Delta E_v + \Delta V \quad (1)$$

where ΔE_v is referred to the difference of the VBM obtained from two independent standard bulk band-structure calculations at the same strained geometries as in the supercell calculation.

ΔV results from the lineup of the macroscopic average of the self-consistent electrostatic potential across the interface. The deduced VBO using the potential-line-up method is calculated to be approximately 0.15 eV, in good agreement with the value from LDOS analysis. As DFT could not reliably determine the conduction band edge due to its limitations in describing excited states, a common method to extract the conduction band offset (CBO) is to use the experimental values of the band gaps. The CBO can then be evaluated using the following equation: CBO = $E_{gBiOCl} - E_{gBi_2WO_6}$ + VBO, where E_{gBiOCl} and $E_{gBi_2WO_6}$ are the experimental optical band gaps. The corresponding CBO value is calculated to be 0.85 eV.

It was reported the first step of photosensibility referred to electrons of excitation dye transferred to the conduction band of the BiOCl[19,42] and Bi_2WO_6.[11] According to the calculated BOs of the BiOCl–Bi_2WO_6 heterojunction, electrons in the conduction band of BiOCl will transfer to the conduction band of Bi_2WO_6 since the latter conduction band position is lower. Meanwhile, additional electrons can be excited to the conduction band of the Bi_2WO_6 under visible light. These transferred and excited electrons could reduce the O_2 to $^{\bullet}O_2^-$ and eventually transform into $^{\bullet}$OH. On the other hand, the holes in the valence band of Bi_2WO_6 transfer to the valence band of BiOCl owing to the higher valence band position of BiOCl and subsequently the holes can oxidize OH^- to $^{\bullet}$OH. The produced $^{\bullet}$OH by both electrons and holes could decompose the RhB. In the whole photosensitized processes, we notice that the holes and electrons are separated to the valence band of BiOCl and

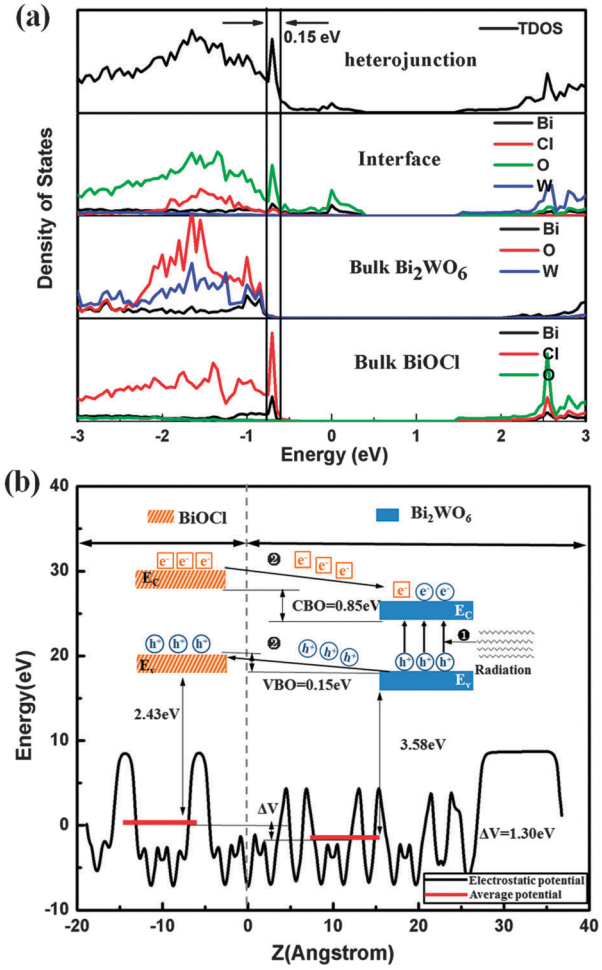

Fig. 7 (a) Calculated TDOS and LDOS for the BiOCl–Bi_2WO_6 interface (b) schematic representation of band offsets for the BiOCl–Bi_2WO_6 interface from the potential-line-up method. Z = 0 denotes the interface.

the conduction band of Bi_2WO_6, respectively. This picture of BOs is favorable for IFCT and efficiently avoids the recombination of electrons and holes in the interface of the BiOCl–Bi_2WO_6 heterojunction (Fig. 7), which contributes to the improved PSDA and PEC performance observed in experiments.

4. Conclusions

We synthesized a hierarchical heterojunction BiOCl–Bi_2WO_6 photocatalyst through a facile one-step solvothermal process. A series of characterization techniques revealed the formation of a heterojunction. The heterojunction yielded enhanced PSDA of RhB (84.6%) under visible light irradiation compared to its individual components. Through the first-principles method, we investigated the detailed terminations of the interface and found that the atomic species could affect the stability of the heterojunction greatly. The calculated BOs show a favorable band alignment for CB-IFCT suppressing the charge carrier recombination, which would benefit enhancement of photosensitized properties. Our theoretical investigations of the heterojunction are consistent with the observed enhanced PSDA of RhB in experiments.

Acknowledgements

This work is supported by the National Basic Research Program of China (2013CB934800 and 2011CB606401), National Natural Science Foundation of China (11004068 and 51101064), Fundamental Research Funds for the Central Universities, HUST (2012TS012 and 2012TS076), and China Postdoctoral Science Foundation (2012M521421). B. Shan would like to acknowledge the support from Program for New Century Excellent Talents in University (NCET). We thank the technology support by the Analytic Testing Center of HUST for carrying out XRD, FESEM and HRTEM analysis and the Texas Advanced Computing Center (TACC) at the University of Texas at Austin (http://www.tacc.utexas.edu) for providing grid resources that have contributed to the research results reported within this paper.

Notes and references

1 M. G. Walter, E. L. Warren, J. R. McKone, S. W. Boettcher, Q. Mi, E. A. Santori and N. S. Lewis, *Chem. Rev.*, 2010, **110**, 6446.
2 X. Chen, S. Shen, L. Guo and S. Mao, *Chem. Rev.*, 2010, **110**, 6503.
3 Y. Q. Lei, G. H. Wang, S. Y. Song, W. Q. Fan and H. J. Zhang, *CrystEngComm*, 2009, **11**, 1857.
4 S. J. Peng, L. L. Li, P. N. Zhu, Y. Z. Wu, M. Srinivasan, S. G. Mhaisalkar, S. Ramakrishna and Q. Y. Yan, *Chemistry*, 2013, **1**, 258.
5 X. Zhang, Z. H. Ai, F. L. Jia and L. Z. Zhang, *J. Phys. Chem. C*, 2008, **112**, 747.
6 L. Q. Ye, K. J. Deng, F. Xu, L. H. Tian, T. Y. Peng and L. Zan, *Phys. Chem. Chem. Phys.*, 2012, **14**, 82.
7 J. Tang, Z. Zou and J. Ye, *Catal. Lett.*, 2004, **92**, 53.
8 M. Shang and W. Z. Wang, *J. Mater. Chem.*, 2009, **19**, 6213.
9 M. Shang, W. Z. Wang, S. M. Sun, L. Zhou and L. Zhang, *J. Phys. Chem. C*, 2008, **112**, 10407.
10 F. Amao, K. Nogami, R. Abe and B. Ohtani, *Chem. Lett.*, 2007, 1314.
11 H. B. Fu, L. W. Zhang, W. Q. Yao and Y. F. Zhu, *Appl. Catal., B*, 2006, **66**, 100.
12 S. Kohtani, M. Koshiko, A. Kudo, K. Tokumura, Y. Ishigaki, A. Toriba, K. Hayakawa and R. Nakagaki, *Appl. Catal., B*, 2003, **46**, 573.
13 M. Shang, W. Z. Wang, J. Ren, S. M. Sun and L. Zhang, *CrystEngComm*, 2010, **12**, 1754.
14 K. R. Lai, Y. T. Zhu, Y. Dai and B. B. Huang, *J. Appl. Phys.*, 2012, **112**, 043706.
15 W. L. Huang and Q. S Zhu, *J. Comput. Chem.*, 2009, **30**, 183.
16 K. L. Zhang, C. M. Liu, F. Q. Huang, C. Zheng and W. D. Wang, *Appl. Catal., B*, 2006, **68**, 125.
17 L. P. Zhu, G. H. Liao, N. C. Bing, L. L. Wang, Y. Yang and H. Y. Xie, *CrystEngComm*, 2010, **12**, 3791.
18 B. O'Regan and M. Grätzel, *Nature*, 1991, **353**, 737.
19 D. H. Wang, G. Q. Gao, Y. W. Zhang, L. S. Zhou, A. W. Xu and W. Chen, *Nanoscale*, 2012, **4**, 7780.
20 U. Bach, D. Lupo, P. Comte, J. E. Moser, F. Weissörtel, J. Salbeck, H. Spreitzer and M. Grätzel, *Nature*, 1998, **395**, 583.
21 J. C. Yu, L. Wu, J. Lin, P. S. Li and Q. Li, *Chem. Commun.*, 2003, 1552.
22 S. Shenawi-Khalil, V. Uvarov, S. Fronton, I. Popov and Y. Sasson, *J. Phys. Chem. C*, 2012, **116**, 11004.
23 S. Khanchandani, S. Kundu, A. Patra and A. K. Ganguli, *J. Phys. Chem. C*, 2013, **117**, 5558.
24 X. Wei, T. F. Xie, L. L. Peng, W. Fu, J. S. Chen, Q. Gao, G. Y. Hong and D. J. Wang, *J. Phys. Chem. C*, 2011, **115**, 8637.
25 J. G. Hou, Z. Wang, C. Yang, W. L. Zhou, S. Q. Jiao and H. M. Zhu, *J. Phys. Chem. C*, 2013, **117**, 5132.
26 F. D. Gao, D. W. Zeng, Q. W. Huang, S. Q. Tian and C. S. Xie, *Phys. Chem. Chem. Phys.*, 2012, **14**, 10572.
27 S. X. Weng, B. B. Chen, L. Y. Xie, Z. Y. Zheng and P. Liu, *J. Mater. Chem. A*, 2013, **1**, 3068.
28 L. Q. Ye, C. Q. Gong, J. Y. Liu, L. H. Tian, T. Y. Peng, K. J. Deng and L. Zan, *J. Mater. Chem.*, 2012, **22**, 8354.
29 W. Zhao, W. H. Ma, C. H. Chen, J. C. Zhao and Z. G. Shuai, *J. Am. Chem. Soc.*, 2004, **126**, 4782.
30 H. F. Cheng, B. B. Huang, X. Y. Qin, X. Y. Zhang and Y. Dai, *Chem. Commun.*, 2012, **48**, 97.
31 W. C. Wang, W. J. Yang, R. Chen, X. B. Duan, Y. L. Tian, D. W. Zeng and B. Shan, *Phys. Chem. Chem. Phys.*, 2012, **14**, 2450.
32 W. Wang, K. Xiong, R. M. Wallace and K. J. Cho, *Appl. Surf. Sci.*, 2010, **256**, 6569.
33 J. P. Perdew, K. Burke and M. Ernzerhof, *Phys. Rev. Lett.*, 1996, **77**, 3865.
34 P. E. Blöchl, *Phys. Rev. B: Condens. Matter Mater. Phys.*, 1994, **50**, 17953.
35 G. Kresse and J. Furthmüller, *Comput. Mater. Sci.*, 1996, **6**, 15.

36 G. Kresse and J. Furthmüller, *Phys. Rev. B: Condens. Matter Mater. Phys.*, 1996, **54**, 8245.
37 W. Press, B. Flannery, S. Teukolsky and W. Vetterling, *Numerical Recipes: The Art of Scientific Computing*, Cambridge University Press, New York, 1986.
38 M. S. Islam, S. Lazure, R. N. Vannier, G. Nowogrocki and G. J. Mairesse, *J. Mater. Chem.*, 1998, **8**, 655.
39 M. S. Gui, W. D. Zhang, Q. X. Su and C. H. Chen, *J. Solid State Chem.*, 2011, **184**, 1977.
40 H. B. Fu, C. S. Pan and W. Q. Yao, *et al.*, *J. Phys. Chem. B*, 2005, **109**, 22432.
41 L. Q. Jing, X. J. Sun, B. F. Xin, B. Q. Wang, W. M. Cai and H. G. Fu, *J. Solid State Chem.*, 2004, **177**, 3375.
42 J. Jiang, K. Zhao, X. Y. Xiao and L. Z. Zhang, *J. Am. Chem. Soc.*, 2012, **134**, 4473.
43 F. Bottin, F. Finocchi and C. Noguera, *Phys. Rev. B: Condens. Matter Mater. Phys.*, 2003, **68**, 035418.
44 K. Reuter and M. Scheffler, *Phys. Rev. B: Condens. Matter Mater. Phys.*, 2001, **65**, 035406.
45 J. M. Bass, M. Oloumi and C. C. Matthai, *J. Phys.: Condens. Matter*, 1989, **1**, 10625.
46 J. Robertson and P. W. Peacock, *Phys. Status Solidi B*, 2004, **241**, 2236.
47 A. Baldereschi, S. Baroni and R. Resta, *Phys. Rev. Lett.*, 1988, **61**, 734.
48 L. Colombo, R. Resta and S. Baroni, *Phys. Rev. B: Condens. Matter Mater. Phys.*, 1991, **44**, 5572.
49 J. Junquera, R. Cohen and K. Rabe, *J. Phys.: Condens. Matter*, 2007, **19**, 203.
50 M. Peressi, N. Binggeli and A. Baldereschi, *J. Phys. D: Appl. Phys.*, 1998, **31**, 1273.

